



1 **Analysis on rock fracture signals and exploration of infrared advance**
2 **prediction under true triaxial loading**

3

4 Jiawang Hao¹, Lan Qiao¹, Zhanjin Li², Qingwen Li¹

5

6 ¹ Beijing Key Laboratory of Urban Underground Space Engineering, University of Science and Technology Beijing,
7 Beijing 100083, China

8 ² School of Mining Engineering, North China University of Science and Technology, Tangshan, Hebei 063210, China

9 **Correspondence**

10 Qingwen Li, Beijing Key Laboratory of Urban Underground Space Engineering, University of Science and Technology
11 Beijing, Beijing, 100083, China. Email: qingwenli@ustb.edu.cn

12 **Funding information**

13 National Natural Science Foundation of China and Shandong province joint program, Grant/Award Numbers:
14 U1806209. Fundamental Research Funds for the Central Universities, Grant/Award Numbers: TP-19-021A3 and FRF-
15 IDRY-19-002.

16

1 **Abstract:** To predict the fractured rock failure under deep triaxial stress in advance, the true triaxial tests were carried
2 out using thermal infrared monitoring and acoustic emission (AE). This paper proposes "infrared temperature jumping
3 rate (ITJR)" to reflect the "jumpiness" of the temperature field matrix, and establishes an infrared advance prediction
4 method. The results show that the high temperature area will converge and expand gradually, and cracks propagate
5 along a certain direction. In the sudden temperature reduction area, the rock stripping is easy to occur. At the boundary
6 between high-low temperature areas, it is easy to produce breakage cracks and form rock spalling. In the short quiet
7 period, the rock gradually gathers strain energy, which will be released in the fracture period. By comparing the time of
8 AE sudden increase with the time of ITJR mutation, it shows that the method has a good advance prediction effect for
9 rock fracture.
10 **Keywords:** true triaxial; infrared temperature field; acoustic emission; interval estimation; advanced prediction.

1 INTRODUCTION

As the excavation of mining engineering, tunnel engineering and water conservancy engineering gradually develops to the deeper region, affected by the original structural in-situ stress and excavation engineering, the stress state under the complex in-situ stress environment in deep underground rock masses is non-isobaric presented as $\sigma_1 > \sigma_2 > \sigma_3$ ¹. In actual underground engineering, the surrounding rock contains a lot of defects such as joints and fissures. Due to the existence of weak geological surface, under the action of stress field, the elastic strain energy gradually accumulates near the primary cracks in the surrounding rock. Due to the non-uniformity of energy accumulation, fractures are prone to occur in the original fissures, leading to engineering disasters such as rock stripping and ejection²⁻⁴. After the excavation, the stress on the rock will redistribute, and the areas near the fissures are more likely to be fractured at this time. Therefore, it is of great theoretical value for the prevention and control of deep underground surrounding rock engineering disasters to study the fracture of fissured rock under the condition of triaxial non-isobaric stress.

The failure of fissured rock under triaxial stress is a process accompanied by energy absorption and release. The failure behavior caused by energy accumulation will release energy to the outside in the form of infrared radiation. As a non-contact observation device, infrared monitoring system can obtain the real-time change of surface rock temperature field in the process of rock failure. Using the infrared monitoring device, the researchers analyzed the characteristics of thermal infrared images and the changes of average infrared radiation temperature in several rock mechanics tests, and found that shear failure can increase the temperature of rock, while tensile failure can lower the temperature of rock⁵⁻⁷. Based on geomechanical model tests, it was found that during the excavation process of rock strata, the infrared temperature increased, and the sporadic distributed high-temperature area gradually evolved into a local distribution near the working face. A method of transforming infrared data by two-dimension Fourier was used to demonstrate the

1 influence of excavation response on rock damage and fracture⁸⁻¹⁰. In the process of rock deformation, the rock will go
2 through compaction stage, elastic stage and plastic stage before reaching the peak stress. By observing the infrared
3 radiation changes of small-sized rock specimen, it was found that the infrared radiation temperature of rock increased
4 slowly and linearly in the elastic stage, while increased rapidly in the plastic stage¹¹. In the cyclic loading and
5 unloading test, the average infrared radiation temperature (AIRT) showed a downward trend in the initial stage, and a
6 sharp increase in the late stage of the test¹². In addition, many researchers have also made great progress in the study of
7 the influence of water content on infrared radiation¹³⁻¹⁶, evaluation of pore characteristic distribution^{17,18} and noise
8 correction of infrared temperature data¹⁹⁻²¹.

9 The above research results of rock fracture by infrared monitoring are basically based on uniaxial compression test
10 or biaxial compression test. Besides, current researches on rock failure under true triaxial stress mainly focus on the
11 mechanical properties of rock²²⁻²⁴, the characteristics of AE signals variation²⁵⁻²⁸, and the law of crack propagation and
12 distribution²⁹⁻³¹. However, very limited research has studied on the thermal infrared radiation of rocks under true triaxial
13 stress loading. Studies have shown that σ_2 has greater influence on rock deformation and failure under the action of
14 triaxial stress³²⁻³⁵. Therefore, this study carried out an actual triaxial test of fissured rock under three types of σ_2 , and
15 found the characteristics of abnormal temperature region in the thermal infrared image (TII), which can obtain the key
16 information of rock fracture in advance. By comparing the time point of the abnormal TII with the time of the sudden
17 increase of AE event, it is preliminarily found that the infrared temperature field has potential value of predicting rock
18 fracture in advance. To quantitatively explore the effect of advance prediction of infrared temperature field, this paper
19 proposed the infrared temperature jumping rate (*ITJR*) to reflect the "jumping" behavior of infrared temperature field.
20 The *ITJR* was derived by differential eliminate noise and variance calculation based on the original temperature field
21 matrix. Through interval estimation and absolute value processing of *ITJR*, the occurrence time of each infrared

prediction under three σ_2 was obtained. By comparing the occurrence time of each infrared prediction with the sudden increase time of AE events, it was found that the infrared prediction based on ITJR was of great value to the prediction of rock fracture in advance. Therefore, this study can provide scientific basis for the prediction of fractured surrounding rock under deep three-direction stress by infrared monitoring technology.

2 BASIC PREPARATION AND TESTING PROCESS

2.1 Rock sample preparation

Red sandstones (Sichuan Province, China) were chosen as the test samples. the samples were processed into 150 mm × 150 mm × 150 mm cubes in accordance with the standards of International Society of Rock Mechanics. To reduce the influence caused by the unevenness of the rock end, the unevenness of the six ends of the red sandstone specimens is limited to less than 0.02 mm. The object of this study is the fractured surrounding rock on the surface of deep roadway, non-penetrating fissures were prefabricated on one end face of samples. To prevent the fissure on the surface from being affected by the loading end effect, the maximum depth of cut should not be too large. In this test, a "chord-shaped" prefabricated fissure with a length of 81.6 mm and a maximum depth of 21.1 mm was cut at the center of the rock. To ensure that the projection length of fissure in the direction of σ_1 and σ_2 are the same, the angle between the prefabricated fissure and the horizontal direction is 45°. To explain the fracture in the area near the prefabricated fissure conveniently, the two tips of the crack are named tip No. 1 and tip No. 2 respectively in Fig. 1.

FIGURE 1 Distribution diagram of prefabricated fissure on red sandstones specimen.

2.2. Experimental system

The experimental system includes true triaxial press, thermal infrared monitoring system and AE monitoring system (Fig.2(a)). The QKX-YB200 true triaxial high servo press was used for the test. The press is composed of five independent loading systems. The Z-axis (applying maximum principal stress) has a maximum load of 3200 KN, the Y-axis (applying intermediate principal stress) and the X-axis (applying minimum principal stress) both have a maximum

1 load of 2400 KN. True triaxial press applies load through oil pump, and the maximum stroke of loading oil cylinder
2 actuator is 200 mm. The PCI-2 type AE detector was used to monitor the real-time AE signal during the fracture of red
3 sandstone. The gain value of preamplifier is 40 dB, and the sampling threshold is 45 dB in the test. The IR8325 type
4 thermal infrared system was used to monitor the changes of real-time temperature field during red sandstone
5 deformation, the infrared sampling rate was 50 SPS/s. Before the test, the samples and the thermal infrared monitoring
6 system must be placed in the press laboratory with constant temperature for at least 24 h in advance to ensure that the
7 temperature of samples and instruments were consistent with the surrounding environment.

8 **2.3 The experimental design and method**

9 The stress of red sandstone in three directions is shown in Fig.2(b). This true triaxial loading test can be divided
10 into the following three steps (Fig. 3). According to the loading rate of 3000 N/s, σ_1 , σ_2 and σ_3 were firstly loaded to
11 state 1 at the same time (hydrostatic pressure $\sigma_1 = \sigma_2 = \sigma_3 = 2.5$ MPa), at this time, σ_3 reached the predefined geostress
12 levels and the loading on σ_3 just remained constant, while σ_1 and σ_2 were continue to be loaded. σ_1 and σ_2 were
13 loaded to state 2 at the same time ($\sigma_2 = \sigma_1$), and σ_2 reached the predefined geostress levels. Then σ_2 stopped loading,
14 σ_1 continued to load to 30 MPa. When $\sigma_1 = 30$ MPa, σ_3 was immediately unloaded (simulating the excavation of
15 underground) as shown in Fig. 2(c). In this study, the predefined geostress levels of σ_2 are 10 MPa, 18 MPa and 26
16 MPa, respectively. Considering that after the deep excavation project is completed, the surrounding rock around the
17 roadway will undergo a period of in-situ stress redistribution. In this study, the load will be maintained for 5 min after

1 unloading σ_3 . After state 2 was completed, the loading rate of 0.12 mm/min was selected to continue to increase σ_1 ,
2 and samples were simultaneously monitored by AE and thermal infrared system. The true triaxial loading path of rocks
3 is shown in Fig. 3. In the study, two experimenters controlled the AE detector and thermal infrared system respectively,
4 and they started simultaneously

5 **FIGURE 2** Description of experimental procedure. (a) experimental system chosen in this study, (b) the stress on six
6 sides of red sandstone, (c) The process of unloading minimum principal stress.

7 **FIGURE 3** True triaxial loading path.

8 **3 ANALYSIS ON THERMAL INFRARED IMAGERY (TII) AND AE SIGNALS**

9 Abnormal temperature areas (ATA) will occur in the deformation process of rock. The real-time infrared
10 temperature field matrixes obtained can be converted into images to accurately obtain the position of rock fracture.
11 During rock fracture, energy is released to the outside in the form of elastic wave. The energy released by the elastic
12 wave in unit time is the energy rate, which can represent the amount of energy released by the rock in unit time, and
13 then reflect the intensity of rock fracture. The number of pulses exceeding the threshold in the AE waveform is AE
14 event, which can reflect the number of fracture events occurring inside the rock at a certain moment. Among the signals
15 representing the deformation characteristics of rock under true triaxial loading, AE count, energy rate, and the
16 maximum infrared radiation temperature (MIRT) were selected in this chapter.

17 **3.1 The evolution of TII during rock deformation**

18 The obtained original infrared temperature field matrix was transformed into TII. To clearly identify the changes of
19 TII in the area near the prefabricated fissure, the position of the prefabricated fissure is added to TII in this paper. Due
20 to the reflection of the metal gasket at the loading end, the position of the prefabricated fissure is not completely in the
21 center of the selected range when selecting the temperature matrix range to generate the TII (to show more detail of TII,
22 the time form is "**.*" in Fig. 4-6).

23 **FIGURE 4** The evolution of TII under intermediate principal stress of 10 MPa.

24 **FIGURE 5** The evolution of TII under intermediate principal stress of 18 MPa.

FIGURE 6 The evolution of TII under intermediate principal stress of 26 MPa.

Fig. 4 shows the evolution of TII in the red sandstone failure process under $\sigma_2 = 10$ MPa. At the beginning of the test ($t=58.5$), there are high-temperature and low-temperature areas on the upper and lower end surfaces of the rock respectively, indicating that the factor causing the temperature change on the rock surface at this time is σ_1 . The high temperature areas on both sides of tip No. 1 are called region 1 and region 2 respectively. When $t=376.2$ s, region 1 had a tendency to gradually expand along the direction of σ_1 incubating fracture events. When $t=434.7$ s, the spread range of region 1 reached the maximum, and the region began to shrink gradually and reached the minimum when $t=564.0$ s. When $t=591.9$ s, region 1 further expanded to the maximum range. In the process of rock deformation, high-temperature region 1 experienced a process of "expansion-contraction-expansion". At this time, a clear high-low temperature boundary appeared near the tip No. 2, which tended to gradually expand.

When $t=602.4$ s, the "tension-shear combination" tiny cracks were generated along the boundary between high and low temperature areas on the rock surface, and a small number of rock fragments were peeled. The high temperature region 1 fractured after reaching the maximum range, which caused the surface rock spalling and induced the formation of tiny cracks at the tip 1. When $t=747.3$ s, a small-scale abnormal high-temperature accumulation area was formed at the tip 2, where the temperature difference was the largest, indicating that more large-scale latent fracture events were forming. At the same time, the high-low temperature boundary at tip No. 1 and the left side of the rock showed further signs of expansion. When $t=796.2$ s, the range of the high temperature accumulation area at tip 2 increased, and the fracture occurred within tip 1 and the high-low temperature boundary on the left side of the rock.

After the accumulation of fracture events for a period of time, until $t=845.7$ s, wide crack formed in the high temperature aggregation area at the tip 2 and a macro-fracture zone was generated. The tip 1 and the area on the left of the rock were further fractured to form a snap crack. At $t=897.7$ s, a high-low temperature area appeared at the lower part of the rock surface, which gradually expanded, overlapped and converged with the snap crack. With the progress of

the test, the fractured areas on the surface of the rock gradually penetrated and coalesced, and rock blocks on the surface were further peeled to form multiple wide cracks ($t=969.6$ s). When $t=1122.3$ s, the corresponding TII was the state after the surface rock fragments peeled off, and it was only presented as a failure demonstration here.

Fig. 5 shows the evolution of TII in the red sandstone failure process under $\sigma_2=18$ MPa. At the beginning of the test ($t=0.3$ s), the high-temperature area and the low-temperature area distributed on the left and right sides of the prefabricated fissure respectively. With the process of loading, the high-temperature area decreased gradually, while the low-temperature area increased gradually ($t=70.5$ s). When $t=270.6$ s, the high-temperature area increased, and the low-temperature area decreased. When $t=348.3$ s and $t=555.9$ s subsequently, similar to the previous image ($t=70.5$ s), the high-temperature area gradually decreased, while the low-temperature area gradually increased. Within the range of $t < 555.9$ s, the change in rock temperature field was caused by σ_1 . Although the surface rock had not formed visible macro-failure, according to the change of "increasing-decreasing-increasing-decreasing" in the low-temperature area on the left of prefabricated fissure, it can be known that the rock was gradually accumulating damage and gestating fracture under the triaxial stress.

Therefore, when $t=636.3$ s, a small range of strip fracture zone appeared near the tip 1, and an abnormally low temperature zone appeared on the right side of the prefabricated fissure. When $t=772.8$ s, the abnormal low-temperature area changed into a strip high-temperature area, which gradually expanded along the direction perpendicular to the prefabricated fissure, leading to many tiny cracks near tip 1. When $t=869.1$ s, the tiny crack near tip 1 was further developed into wide crack, and a strip-shaped high-low temperature boundary appeared at the lower left of the prefabricated fissure. The expansion direction of the strip-shaped high-temperature zone on the right side of the prefabricated fissure ($t=772.8$ s) had been changed and pointed to the direction of the tip 2. The small-scale high-temperature accumulation area at the tip 2 had developed along the high-temperature points toward a and b.

When $t=886.6$ s, the strip high-temperature area ($t=869.1$ s) pointing to tip 2 occurred rock fragmentation and incubated tiny cracks, and the two directions of the downward-expanding high-temperature area at tip 2 changed

1 slightly. The strip-shaped high and low temperature boundary previously appeared ($t=869.1$ s) at the lower left of the
2 prefabricated fissure were more obvious at this time. The expansion direction (a and b) of the high-temperature area at
3 tip 2 changed again. When $t=997.1$ s, under the influence of a larger σ_2 , a wide crack along the direction towards a was
4 finally formed at tip 2. The wide crack along the strip-shaped high and low temperature boundary was formed at the
5 lower left of the prefabricated fissure. When $t=1125.3$ s, the corresponding TII is the state after the surface fragments
6 spalling, and it was only shown as a failure demonstration here.

7 Fig. 6 shows the evolution of TII in the red sandstone failure process under $\sigma_2=26$ MPa. In the early stage of the
8 test, the infrared temperature field of the rock did not change significantly, until $t=352.5$ s, most of the rock surface was
9 in a high-temperature area. When $t=426$ s, the location of the high-temperature area was basically the previous low
10 temperature area, and there was an abnormal long strip-shaped temperature boundary on the right of tip No. 2. Similar
11 to other specimens, high and low temperature zones appeared alternately in the same area with the progress of loading,
12 indicating that the rock was gradually accumulating damage and gestating deformation.

13 When $t=835.7$ s, the long strip-shaped temperature boundary zone gradually shrank, and the high-temperature
14 aggregation area at tip 1 gradually expanded to the upper part of the rock, accompanied by the appearance of fine crack
15 at the upper left corner. At $t=860.1$ s, the high-temperature aggregation area at tip 1 was fractured, forming a tiny crack
16 that started from tip 1 and was approximately perpendicular to the prefabricated fissure. An abnormally low-
17 temperature area appeared below the prefabricated fissure, indicating that fracture events may occur in this area. The
18 long strip-shaped temperature boundary zone gradually expanded to both sides. When $t=927.6$ s, there were a large area
19 of rockslide and spalling beneath the prefabricated fissure. The long strip-shaped temperature boundary zone reached
20 the maximum and gradually shrank. At $t=948.9$ s, a high-temperature aggregation area was formed at tip 2, and this area
21 was gestating the expansion path under external load.

22 When $t=960$ s, the high-temperature area at tip 2 was fractured, forming a tiny crack that expanded to the left. Due

1 to the higher σ_2 in the lateral direction of the specimen, the angle between tiny crack and the trend of prefabricated
2 fissure was greater than 90° . The high-temperature area formed at the lower right of the rock gradually expanded
3 towards tip 2. The high-temperature area on the right side of tip 1 showed signs of rightward expansion, which included
4 directions towards a and b. When $t=983.4$ s, under the influence of σ_1 , the propagation direction of the tiny crack at tip
5 2 changed, forming a wide crack approximately 90° to the prefabricated fissure. The high-temperature area fractured in
6 the lower right of the rock. The high temperature area on the right of tip 1 formed tiny crack approximately along the
7 direction a. When $t=1048.2$ s, flaking of rock fragments occurred on a large area of rock surface. When $t=1080.3$ s, the
8 corresponding TII is the state after the surface rock fragments peeling off, and it was only shown as a failure
9 demonstration here.

10 According to the evolution process of TII transformed by the temperature field matrix under three kinds of σ_2 ,
11 before the macro-fracture of the rock is visible to eyes, the temperature field of the surface rock changes dramatically
12 under the influence of σ_2 . Before the fracture occurs in a certain area, there will be a high temperature aggregation area.
13 The stress in the area will be released after fracture occurs, causing rapid temperature changes. The explanation
14 regarding to the internal mechanism of fracture easily occurring in the high-temperature accumulation area in Fig. 4-6,
15 is presented as follows.

16 According to the existing studies³⁶, the principal stress of the rock has the following relationship with the thermal
17 infrared signals in the process of external loading.

$$\Delta\sigma_1 = \frac{DGRS}{2048TeK} \quad (1)$$

19 where, σ_1 is the principal stress on the rock (MPa), D is the reflecting temperature of the thermal infrared system
20 ($K \cdot V^{-1}$), G is the instrument sensitivity (V), R is the temperature correction factor, S is the thermoelastic signal of the

1 system (U), T is the absolute temperature of the measured area (K), e is the rock emissivity, and K is the
2 thermoelastic coefficient.

3 According to fracture mechanics, the fracture strength σ_f at the prefabricated fissure tip is as follows.

$$4 \quad \sigma_f = \sqrt{\frac{E\gamma}{4a}} \quad (2)$$

5 where E is young's elastic modulus, γ is surface energy, and a is 1/2 of the length of prefabricated fissure.

6 Let the ratio of σ_f to $\Delta\sigma_1$ be the stress concentration factor β , which has the following relationship from
7 formulas (1) and (2).

$$8 \quad \beta = \frac{\sigma_f}{\Delta\sigma_1} = \frac{1024TeK\sqrt{\frac{E\gamma}{4a}}}{DGRS} \quad (3)$$

9 From formula (3), β and T have a positive correlation. The increase of T in a certain area of the rock indicates
10 that there is a significant stress concentration phenomenon in this area, and the rock is prone to crack and expand along
11 the direction of stress concentration. The crack propagation phenomenon is caused by the release of elastic strain
12 energy, and the release of energy will further cause the temperature rise. In summary, according to the location of the
13 abnormal temperature area and the expansion direction of the high-temperature area in the real-time TH, key fracture
14 information such as the rock fracture location, crack expansion direction, and flake spalling range can be obtained in
15 advance.

16 3.2 The analysis on time domain signals of AE and infrared

17 3.3 Real-time precursor signals characteristics of AE

18 Fig. 7 shows the evolution of multi-parameter signals during the red sandstone failure under $\sigma_2 = 10$ MPa.
19 According to the interval where AE event and energy rate have consistent changes, it can be divided into the quiet
20 period and the fracture period. The failure of rocks had experienced "quiet period-fracture period-short quiet

1 period-fracture period-short quiet period-fracture period". During the quiet period, a small number of fracture
2 events occurred inside the rock. Only when $t=604.96$ s, a fracture with high energy rate occurred. The curves of
3 cumulative energy rate and cumulative AE events rose gently during this period. In the range of the fracture
4 period, a large number of fracture events with high energy rate occurred inside the rock, and the curves of
5 cumulative energy rate and cumulative AE events presented a step-like surge. In the short quiet period between
6 interval I and interval II, although there were fewer fracture events and lower energy release rate, elastic strain
7 energy gradually accumulated in this period (corresponding to the gradual expansion of the high-temperature area
8 in Fig. 4). A large amount of energy accumulated inside the rock was gradually released in the interval II, forming
9 the cluster-events with higher energy release rate.

10 **FIGURE 7** The evolution of multi-parameter signals during rock deformation ($\sigma_2=10$ MPa).

11 Fig. 8 shows the evolution of multi-parameter signals during the red sandstone failure under $\sigma_2=18$ MPa. The
12 rock experienced two "short quiet period-fracture period" processes, after undergoing the "quiet period-fracture period-
13 short quiet period-fracture period". Compared with Fig. 7, the rock at higher lateral σ_2 experienced more "short quiet
14 period" to accumulate elastic strain energy. During the quiet period, compared with the specimen under $\sigma_2=10$ MPa, the
15 number of fracture events and the energy release rate inside the rock were reduced. After the end of the first two short
16 quiet periods, the energy accumulated inside the rock was quickly released in interval III, resulting in a large number of
17 cluster-events with higher energy release rate.

18 **FIGURE 8** The evolution of multi-parameter signals during rock deformation ($\sigma_2=18$ MPa).

19 Fig. 9 shows the evolution of multi-parameter signals during the red sandstone failure under $\sigma_2=26$ MPa. The
20 number of short quiet periods and fracture periods experienced by the rock is the same as that in Fig. 8. During the quiet

1 period on the left side of interval I, there were few fracture events inside the rock and the energy release rate was very
2 low. It showed that increasing σ_2 will restrain the initiation of micro-cracks in the rock during the linear elastic stage.
3 Due to the highest value of σ_2 in this specimen, more elastic strain energy was accumulated inside the rock in each
4 short quiet period, resulting in a large number of cluster-events with higher energy release rate during the next fracture
5 period (II, III and IV). Therefore, the curves of cumulative energy rate and cumulative AE events showed a sudden rise.
6 **FIGURE 9** The evolution of multi-parameter signals during rock deformation ($\sigma_2=26$ MPa).

7 **3.4 Infrared prediction before rock fracture**

8 The above makes necessary analysis on the characteristics change of AE event and energy rate during rock
9 deformation under true triaxial conditions. In the process of rock failure, the rock experienced one quiet period, several
10 short quiet periods and fracture periods. The method of dividing the deformation process into several periods by stages
11 seems to provide guidance for the prediction of surrounding rock fracture under deep three-direction stress. However,
12 AE event and energy rate are the monitoring results after the rock has fractured. When a large number of cluster-events
13 with higher energy rate occur, the rock has already broken, which corresponds to rock burst and rib spalling and other
14 disasters of on-site engineering. Therefore, it is not practical to take only the abnormal characteristics of AE signals as
15 the basis of rock fracture prediction.

16 AE events refer to the number of overall rock fracture events, and the object of infrared monitoring is the surface
17 rock. As shown in Fig. 10, most parts of the rock (internal parts) under true triaxial stress will be restricted (stress on 6
18 faces) by the horizontal σ_3 of surface rock, which will restrain the crack initiation of internal rock to some extent.

19 Because the surface rock has no lateral restriction in the direction of σ_3 (stress on 5 faces), the rock is prone to
20 dilatation, deformation and fracture at the free surface. Therefore, compared with the method of AE monitoring the

overall rock fracture (mainly the internal rock fracture), the infrared monitoring method can obtain the information of rock surface fracture in advance. In Fig. 7-9, the MIRT corresponding to each abnormal TII is either a high temperature value or a low temperature value. Obviously, MIRT cannot be used as the reference parameter for prediction. In this study, by combining abnormal TII with the evolution process of multi-parameter signals, it is found that abnormal TII can predict most fracture events in advance (at this time, AE event and energy rate will increase suddenly). Abnormal TII has potential value of predicting rock fracture in advance. The analysis is as follows.

FIGURE 10 Difference in stress between surface rock and internal rock.

In the quiet period in Fig. 7, at $t=424.13$ s and $t=604.96$ s, a small number of fracture events shown by AE event and energy rate can be predicted in advance by the abnormal TII at $t=376.27$ s and $t=591.92$ s respectively. Similarly, a large number of cluster-events with higher energy rate in the fracture period I, II and III can be predicted by abnormal TII at $t=747.34$ s, 897.76 s and 1122.35 s, respectively.

In the quiet period in Fig. 8, at $t=371.87$ s, a small number of fracture events shown by AE event and energy rate can be predicted in advance by the abnormal TII at $t=270.65$ s respectively. Similarly, a large number of cluster-events with higher energy rate in the fracture period I and II can be predicted by abnormal TII at $t=772.87$ s and 869.12 s, respectively.

In the quiet period in Fig. 9, at $t=435.22$ s, a small number of fracture events shown by AE event and energy rate can be predicted in advance by the abnormal TII at $t=426.00$ s. Similarly, a large number of cluster-events with higher energy rate in the fracture period I, II, III and IV can be predicted by abnormal TII at $t=835.77$ s, 927.65 s, 983.49 s and 1080.33 s, respectively.

4 INFRARED FORWARD PREDICTION BASED ON INFRARED TEMPERATURE JUMPING RATE (ITJR)

When the thermal infrared system is used to monitor the deep fractured surrounding rock under triaxial stress, it is of great significance for the prevention and control of deep disaster accidents to establish the response mechanism of

fracture prediction based on a certain parameter after calculation. From the above preliminary analysis on TII, it can be seen that abnormal TII has the potential value to predict rock fracture in advance. However, the formation of abnormal TII is the result of the accumulation of temperature field matrix at the previous moment. Therefore, what extent of TII mutation as a certain parameter to predict fracture events requires further analysis. In this paper, the differential temperature field matrix after removing noise is calculated. By calculating the variance of the real-time temperature field matrix, an infrared temperature jumping rate (*ITJR*) reflecting the law of the real-time temperature field is proposed. Based on the interval estimation theory in statistical mathematics, the *ITJR* threshold for infrared prediction is obtained. After comparing the time of *ITJR* that exceeds the threshold (the time of infrared prediction) with the time of AE event uprush, it is found that the infrared prediction based on *ITJR* has a good effect in advance prediction.

The mathematical essence of TII is the numerical matrix of temperature field. To reduce the influence of environmental factors and the difference in the emissivity of each part of red sandstone on the error of the temperature matrix, it is necessary to perform the difference calculation of the original temperature field matrix obtained in real time in the test, so as to obtain the differential temperature field matrix $\varphi_k(x, y)$ after removing the interference factors.

$$\varphi_k(x, y) = W_k(x, y) - W_1(x, y) \quad (4)$$

where, $W_k(x, y)$ is the k -th original temperature field matrix, $W_1(x, y)$ is the first original temperature field matrix,

(x, y) is the space coordinate, x and y are the number of rows and columns of the temperature field matrix respectively.

To quantitatively analyze the alienation phenomenon of infrared radiation temperature field of red sandstone under

true triaxial loading, the real-time variance S_i^2 of differential infrared temperature field is obtained using statistical

mathematics. The change of S_i^2 can accurately reflect the deviation degree of temperature field of rock surface away

from the average temperature in the deformation process.

$$S_t^2 = \frac{1}{M} \frac{1}{N} \sum_{j=1}^N \sum_{i=1}^M [\varphi_k(x, y) - AIRT_k]^2 \quad (5)$$

$$AIRT_k = \frac{1}{M} \frac{1}{N} \sum_{j=1}^N \sum_{i=1}^M [\varphi_k(x, y)]^2 \quad (6)$$

$AIRT_k$ is the average infrared radiation temperature of the k -th temperature field, and M and N are the largest rows and columns in the temperature field matrix respectively.

Fig. 11 shows the change of S_t^2 during rock deformation under $\sigma_2=10$ MPa, 18 MPa and 26 MPa. The S_t^2 can be divided into two stages according to the pre-peak and post-peak of the mechanical curve. Before the peak of σ_1 , the S_t^2 of the specimen under $\sigma_2=10$ MPa showed a horizontal fluctuation, while the S_t^2 of the specimen under $\sigma_2=18$ MPa and 26 MPa showed a downward trend. After σ_1 reached its peak value, the S_t^2 of specimens under $\sigma_2=10$ MPa and 18 MPa showed a rapid increase, while the S_t^2 of specimen under $\sigma_2=26$ MPa showed a rapid decrease.

FIGURE 11 The variance of the difference infrared temperature field. (a) $\sigma_2=10$ MPa, (b) $\sigma_2=18$ MPa, (c) $\sigma_2=26$ MPa.

There are many jumping points in real-time S_t^2 in Fig. 11. The "jump" behavior of S_t^2 corresponds to the sharp change of the infrared temperature field matrix (abnormal TII). Infrared temperature jumping Rate (*ITJR*) was defined in this study as a reference parameter for quantitative analysis on the "jumping" behavior of infrared temperature field.

ITJR is derived from the S_t^2 and time interval Δt of the difference temperature field matrix.

$$ITJR_i = \frac{S_{i+\Delta t}^2 - S_i^2}{\Delta t} \quad (7)$$

When studying the infrared prediction of rock fracture, it is necessary to select the range of time. When the stress reaches the peak strength, large-scale fracture events have occurred, and the rock has become unstable. Infrared prediction has no practical significance at this time. Therefore, it is worthwhile to select the time interval before the peak stress as the analysis range. Fig. 12 is the distribution diagram of *ITJR*, and the figure can highlight the statistical distribution and structural features of *ITJR*. When *ITJR* is a positive value, it indicates that the temperature at a certain moment is higher than that at the previous moment.

When establishing the prediction range of *ITJR*, it is necessary to remove most of the irrelevant data based on the data in Fig. 12 and select the threshold value of *ITJR*. If the threshold is too large, some *ITJR* data (signal that surface rock is about to flake) that have undergone large changes in some temperature fields will fall within the threshold, and infrared forecast is barely possible. If the threshold value is too small, some *ITJR* data with small changes in temperature fields will fall outside the threshold value, triggering infrared pre-warning and resulting in invalid infrared prediction. After analyzing the distribution characteristics of *ITJR* data, it is found that *ITJR* approximately meets the normal distribution (Fig. 13). Therefore, it is necessary to use the interval estimation theory to eliminate irrelevant data.

FIGURE 12 The distribution of *ITJR*. (a) $\sigma_2=10$ MPa, (b) $\sigma_2=18$ MPa, (c) $\sigma_2=26$ MPa.

FIGURE 13 Frequency distribution histogram of *ITJR*. (a) $\sigma_2=10$ MPa, (b) $\sigma_2=18$ MPa, (c) $\sigma_2=26$ MPa.

According to the interval estimation theory, the algorithms of normal distribution are as follows.

$$f_{(x)} = \frac{1}{\sqrt{2\pi}\sigma} \exp \left(-\frac{(x-\mu)^2}{2\sigma^2} \right) \quad (8)$$

$$U = \frac{\bar{X} - \mu}{\sigma / \sqrt{n}} \sim N(0, 1) \quad (9)$$

$$P\left[\underline{\theta} < \mu < \bar{\theta} \right] = 1 - \alpha \quad (10)$$

$$\begin{cases} \underline{\theta} = \bar{X} - \frac{\sigma}{\sqrt{n}} u_{\alpha/2} \\ \bar{\theta} = \bar{X} + \frac{\sigma}{\sqrt{n}} u_{\alpha/2} \end{cases} \quad (11)$$

where, $f_{(x)}$ is the probability density function, σ is the standard deviation, μ is the mathematical expectation, U is the sample value, n is the sample size, \bar{X} is the sample mean, $1-\alpha$ is the confidence level (reliability), $N(0,1)$ is the standard normal distribution, $(\underline{\theta}, \bar{\theta})$ is the confidence interval.

$$\begin{cases} f_{(x)} = \frac{1}{1.34 \times 10^{-4} \sqrt{2\pi}} e^{-\frac{[x - (2.93 \times 10^{-7})]^2}{3.60 \times 10^{-8}}} (\sigma_2 = 10 \text{MPa}) \\ f_{(x)} = \frac{1}{3.24 \times 10^{-4} \sqrt{2\pi}} e^{-\frac{[x + (5.99 \times 10^{-7})]^2}{2.10 \times 10^{-7}}} (\sigma_2 = 18 \text{MPa}) \\ f_{(x)} = \frac{1}{6.16 \times 10^{-4} \sqrt{2\pi}} e^{-\frac{[x - (1.46 \times 10^{-7})]^2}{7.59 \times 10^{-7}}} (\sigma_2 = 26 \text{MPa}) \end{cases} \quad (12)$$

$$\begin{cases} (\underline{\theta}, \bar{\theta})_{\sigma_2=10 \text{MPa}} = (-7.76, 8.35) \times 10^{-6} \\ (\underline{\theta}, \bar{\theta})_{\sigma_2=18 \text{MPa}} = (-1.89, 1.77) \times 10^{-5} \\ (\underline{\theta}, \bar{\theta})_{\sigma_2=26 \text{MPa}} = (-3.36, 3.39) \times 10^{-5} \end{cases} \quad (13)$$

The confidence level should be increased as much as possible to eliminate more irrelevant data points (interference points). Therefore, let $1-\alpha = 99.99\%$, then $\alpha = 0.0001$ and $\alpha/2 = 0.00005$, according to the query standard normal distribution table, $u_{\alpha/2} = 3.08$. Because the number of *ITJR* data points obtained by the three specimens is different (there are many irrelevant data points when $\sigma_2=10$ MPa and 18 MPa), after repeated calculation, it is found that the *ITJR* data obtained under $\sigma_2=26$ MPa need to be performed once interval estimation. For the *ITJR* data obtained under

1 $\sigma_2=10$ MPa and 18 MPa, three times interval estimation are required. The specific idea is as follows: after the
2 completion of the first interval estimation, the data points within the confidence level are eliminated, the data points on
3 the left side of the confidence interval (negative value) subtract the lower limit of the confidence interval, and the data
4 points on the right side (positive value) subtract the upper limit of the confidence interval. At this time, the data points
5 obtained still approximately meet the normal distribution. And so on, the final confidence interval is obtained. The
6 following are the probability density function and confidence interval of *ITJR* data points under three kinds of σ_2 after
7 once interval estimation.

8 The data points outside the final confidence interval are recovered numerically (both positive and negative values
9 are added to the previously subtracted values). Thus, a series of effective *ITJR* data points that can reflect the
10 characteristic of rapid change of infrared temperature field are obtained. To show the change distribution of *ITJR*
11 intuitively, the *ITJR* data points after the numerical recovery are treated with the absolute value, and the $|ITJR|$ threshold
12 value of each specimen is marked. Fig. 14 shows the time of each $|ITJR|$ prediction position of each specimen. To
13 demonstrate the value of infrared advance prediction based on *ITJR*, this study chose the internationally recognized AE
14 event and $|ITJR|$ for comparison.

15 **FIGURE 14** The occurrence time of several infrared predictions. (a) $\sigma_2=10$ MPa, (b) $\sigma_2=18$ MPa, (c) $\sigma_2=26$ MPa.

16 Because the deformation of the rock is a gradual failure process stemmed from small-scale fracture events to
17 larger-scale fracture events. Therefore, when selecting the sudden increase point of AE before the peak stress, the
18 number of AE events at the time should be greater than the number of events at any previous time. Table 1 shows the
19 comparison of the time of infrared prediction and AE prediction of rock fracture under three types of σ_2 . When $\sigma_2=10$
20 MPa, three times of rock fracture occurred before the peak stress. The AE event showed three times increase, and the
21 corresponding time was 424.13 s, 604.96 s and 792.40 s respectively. The start time of infrared $|ITJR|$ is 296.98 s,

602.08 s and 736.78 s respectively, which are earlier than the AE event and successfully achieved the advanced prediction of rock fracture. When $\sigma_2=18$ MPa, there were three times successful infrared advance predictions for the four times sudden increase of AE event of rock fracture, and the fourth sudden increase of infrared $|ITJR|$ is only 0.82 s behind the AE event. When $\sigma_2=26$ MPa, there were two times successful infrared advance predictions for the three times sudden increase of AE event of rock fracture, and the third sudden increase of infrared $|ITJR|$ is 8.94 s behind the AE event. This is because when the stress is about to reach the peak strength, rock is experiencing the plastic deformation, and the anisotropic group-cracks distributed in the internal space of the rock are in the state of unstable expansion. AE will obtain the occurrence of a large number of fracture events in advance. Therefore, near the peak strength, the infrared advanced prediction based on $ITJR$ may be biased.

TABLE 1 Comparison of infrared and AE prediction time of rock fracture

The key to utilize the infrared prediction method proposed in this study is that when the first infrared prediction occurs (Fig. 15), corresponding measures will be adopted to prevent the subsequent deformation and the failure of surrounding rocks (nip in the bud), so that surrounding rock will not fracture further. When $|ITJR|$ does not exceed the threshold value at a certain moment, the prediction will not be triggered, and the construction work and infrared monitoring will continue. When $|ITJR|$ exceeds the threshold at a certain moment, the prediction will be triggered, and constructors and equipment are required to leave the working area immediately. The treatment methods adopted are as follows: changing the parameters of the stress release holes (position, hole depth and spacing) to relieve the stress concentration in surrounding rock, decreasing the excavating velocity of the tunnel face to reduce the engineering disturbance. Then, the support system is optimized on the basis of the previous support to secure the safety of the actual fractured areas and the potential fractured areas in TII.

FIGURE 15 Response mechanism of infrared advance prediction of fractured rock masses under deep three-direction stress.

1 **5 CONCLUSIONS**

2 (1) In the early stage of the test, the "stress infrared radiation effect" caused by stress will cause the area of the
3 high-temperature and low-temperature to increase or decrease alternately. When σ_2 increases, it will promote the
4 initiation crack at the tip of the prefabricated fissure to develop in the horizontal direction (restrain initial crack to
5 expand upward), and gradually increase the angle between the crack propagation direction and the vertical direction,
6 indicating the magnitude of σ_2 has a great influence on the rock fracture. Meanwhile, the mechanism of crack extension
7 along high temperature zone can be well explained from the theoretical analysis.

8 (2) During the failure process, specimens experienced a quiet period, several short quiet periods and fracture
9 periods. The increase of σ_2 will restrain the cracks initiation inside the rock, so there are fewer fracture events during
10 the quiet period. A high σ_2 will improve the rock's ability to store strain energy in short quiet period, and subsequent
11 release of energy will easily lead to a large number of cluster-events with higher energy rate in the fracture period.

12 (3) On the basis that abnormal TII can preliminarily predict rock fracture, *ITJR* which reflects the "jump" behavior
13 of temperature field matrix is proposed. Using statistical mathematics methods, interval estimation is performed for
14 *ITJR* data that meet the normal distribution, and the occurrence time of several infrared predictions are obtained under
15 three kinds of σ_2 before the peak strength of rock. By comparing the occurrence time of infrared prediction and the
16 sudden increase time of AE event, it is found that the method of infrared prediction based on *ITJR* has a better effect of
17 advance prediction.


18 **ACKNOWLEDGEMENT**


1 The authors would like to acknowledge the support from the National Natural Science Foundation of China and
2 Shandong province joint program (U1806209) and the Basic Scientific Research Operating Expenses of Central
3 Universities (FRF-TP-19-021A3 and FRF-IDRY-19-002).

4 NOMENCLATURE

5 CT Computed tomography

6 ORCID

7 Jiawang Hao  <https://orcid.org/0000-0001-6787-7913>

8 Qingwen Li  <https://orcid.org/0000-0002-2271-1036>

9 Data Availability Statement

10 The data that support the findings of this study are available from the corresponding author upon reasonable request.

11 REFERENCES

- 12 1. Brace WF, Kohlstedt DL. Limits on lithospheric stress imposed by laboratory experiments. *J Geophys Res-Atmos.*
13 1980;85(B11):6248-6252.
- 14 2. Zhou XP, Cheng H, Feng YF. An experimental study of crack coalescence behaviour in rock-like materials
15 containing multiple flaws under uniaxial compression. *Rock Mech. Rock Eng.* 2014;47, 1961-1986.
- 16 3. Feng P, Dai F, Liu Y, Xu NW, Fan PX. Effects of coupled static and dynamic strain rates on mechanical behaviors
17 of rock-like specimens containing pre-existing fissures under uniaxial compression. *Can. Geotech. J.* 2018;55(5),
18 640-652.
- 19 4. Feng P, Dai F, Liu Y, Xu NW, Du HB. Coupled effects of static-dynamic strain rates on the mechanical and
20 fracturing behaviors of rock-like specimens containing two unparallel fissures. *Eng. Fract. Mech.* 2019;207, 237-
21 253.
- 22 5. Wu LX, Liu SJ, Wu YH, Wu HP. Changes in infrared radiation with rock deformation. *Int J Rock Mech Min Sci.*

2002;39(6):825-831.

6. Wu LX, Liu SJ, Wu YH, Wang CY. Precursors for rock fracturing and failure—Part I: IRR image abnormalities. *Int J Rock Mech Min Sci.* 2006(a);43(3):473-482.

7. Wu LX, Liu SJ, Wu YH, Wang CY. Precursors for rock fracturing and failure—Part II: IRR T-Curve abnormalities. *Int J Rock Mech Min Sci.* 2006(b);43(3):483-493.

8. He MC, Gong WL, Zhai HM, Zhang HP. Physical modeling of deep ground excavation in geologically horizontal strata based on infrared thermography. *Tunn Undergr Sp Tech.* 2010;25(4):366-376.

9. He MC. Physical modeling of an underground roadway excavation in geologically 45° inclined rock using infrared thermography. *Eng Geol.* 2011;121(3-4):165-176.

10. Gong WL, He MC, Yan H, Li LF, Xu XD. Geomechanical Model Tests and Infrared Detection of Rock Responses for Tunnels Excavated in Sedimentary Rocks. *Procedia Eng.* 2017;191:20-30.

11. Sun XM, Xu HC, He MC, Zhang F. Experimental investigation of the occurrence of rockburst in a rock specimen through infrared thermography and acoustic emission. *Int J Rock Mech Min Sci.* 2017;93:250-259.

12. Cao KW, Ma LQ, Wu Y, Khan NM, Spearing AJS, Hussain S, Yang J. Cyclic fatigue characteristics of rock failure using infrared radiation as precursor to violent failure: Experimental insights from loading and unloading response. *Fatigue Fract. Eng. Mater. Struct.* 2021;44(2): 584-594.

13. Liu XX, Liang ZZ, Zhang YB, Liang P, Tian BZ. Experimental study on the monitoring of rockburst in tunnels under dry and saturated conditions using AE and infrared monitoring. *Tunn Undergr Sp Tech.* 2018;82:517-528.

14. Ma LQ, Zhang Y, Cao KW, Wang ZW. An experimental study on infrared radiation characteristics of sandstone samples under uniaxial loading. *Rock Mech Rock Eng.* 2019;52(9):3493-3500.

15. Xiao FK, He J, Liu ZJ, Shen ZL, Liu G. Analysis on warning signs of damage of coal samples with different water contents and relevant damage evolution based on acoustic emission and infrared characterization. *Infrared Phys Techn.* 2019;97:287-299.

16. Shen RX, Li HR, Wang EY, Chen TQ, Li TX, Tian H, Hou ZH. Infrared radiation characteristics and fracture precursor information extraction of loaded sandstone samples with varying moisture contents. *Int J Rock Mech*

1 *Min Sci.* 2020;130:104344.

2 17. Mineo S, Pappalardo G. The use of infrared thermography for porosity assessment of intact rock. *Rock Mech Rock*
3 *Eng.* 2016;49:3027–3039.

4 18. Pappalardo G, Mineo S. Investigation on the mechanical attitude of basaltic rocks from Mount Etna through
5 InfraRed Thermography and laboratory tests. *Constr Build Mater.* 2017;134:228-235.

6 19. Ozsarac S, Akar GB. Atmospheric effects removal for the infrared image sequences. *IEEE Trans. Geosci. Remote*
7 *Sens.* 2015;58(9), 4899-4909.

8 20. Sun H, Ma LQ, Adeleke N, Zhang Y. Background thermal noise correction methodology for average infrared
9 radiation temperature of coal under uniaxial loading. *Infrared Phys. Techn.* 2017;81, 157-165.

10 21. Liu, L., Xu, L.P. & Fang, H.Z. Simultaneous intensity bias estimation and stripe noise removal in infrared images
11 using the global and local sparsity constraints. *IEEE Trans. Geosci. Remote Sens.* 2020;58(3), 1777-1789.

12 22. Chang CD, Haimson B. True triaxial strength and deformability of the German Continental Deep Drilling Program
13 (KTB) deep hole amphibolite. *J Geophys Res-Atmos.* 2000;105(B8):18999-19013.

14 23. Lee H, Haimson B. True triaxial strength, deformability, and brittle failure of granodiorite from the San Andreas
15 Fault Observatory at Depth. *Int J Rock Mech Min Sci.* 2011;48(7):1199-1207.

16 24. Zhao J, Feng XT, Zhang XW, Zhang Y, Yang CX. Brittle-ductile transition and failure mechanism of jinping
17 marble under true triaxial compression. *Eng Geol.* 2018;232:160-170.

18 25. He MC, Miao JL, Feng JL. Rock burst process of limestone and its acoustic emission characteristics under true-
19 triaxial unloading conditions. *Int J Rock Mech Min Sci.* 2010;47(2):286-298.

20 26. Zhao XG, Wang J, Cai M, Cheng C, Ma LK, Su R, Zhao F, Li DJ. Influence of unloading rate on the strainburst
21 characteristics of Beishan granite under true-triaxial unloading conditions. *Rock Mech Rock Eng.* 2014;47:467-
22 483.

23 27. Zhu GA, Dou LM, Wang CB, Ding ZW, Feng ZJ, Xue F. Experimental study of rock burst in coal samples under
24 overstress and true-triaxial unloading through passive velocity tomography. *Safety Sci.* 2019;117:388-403.

25 28. Feng XT, Gao YH, Zhang XW, Wang ZF, Zhang Y, Han Q. Evolution of the mechanical and strength parameters

of hard rocks in the true triaxial cyclic loading and unloading tests. *Int J Rock Mech Min Sci.* 2020;131:104349.

29. Zheng Z, Feng XT, Yang CX, Zhang XW. Post-peak deformation and failure behaviour of Jinping marble under true triaxial stresses. *Eng Geol.* 2019;265:105444.

30. Wang SS, Xu WY, Yan L, Feng XT, Xie WC, Chen HJ. Experimental investigation and failure mechanism analysis for dacite under true triaxial unloading conditions. *Eng Geol.* 2020;264:105407.

31. Du K, Yang CZ, Su R, Tao M, Wang SF. Failure properties of cubic granite, marble, and sandstone specimens under true triaxial stress. *Int J Rock Mech Min Sci.* 2020;130:104309.

32. Mogi K. Effect of the intermediate principal stress on rock failure. *J Geophys Res.* 1967;72(20):5117-5131.

33. Cai M. Influence of intermediate principal stress on rock fracturing and strength near excavation boundaries-Insight from numerical modeling. *Int J Rock Mech Min Sci.* 2008;45(5):763-772.

34. Pan PZ, Feng XT, Hudson JA. The influence of the intermediate principal stress on rock failure behaviour: A numerical study. *Eng Geol.* 2012;124:109-118.

35. Feng XT, Zhang XW, Kong R, Wang G. A novel mogi type true triaxial testing apparatus and its use to obtain complete stress-strain curves of hard rocks. *Rock Mech Rock Eng.* 2016;49(5):1649-1662.

36. Barone S, Patterson EA. The development of simultaneous thermo-and photo-elasticity for principal stress analyses. *Strain.* 1999;35(2):57-65.

1 **Highlights**

- 2 (1) Before the rock fracture, abnormal temperature areas will appear.
- 3 (2) The key information of rock fracture can be obtained in advance based on ATA.
- 4 (3) The abnormal TII can predict the occurrence of fracture events earlier than AE.
- 5 (4) This paper proposes an infrared advanced prediction method.